TID-4500, UC-35
Nuclear Explosions—
Peaceful Applications

Lawrence Radiation Laboratory
UNIVERSITY OF CALIFORNIA
LIVERMORE

UCRL-50898
IOCS-CC-15

NUCLEAR CRATERING ON A DIGITAL COMPUTER

R. W. Terhune
T. F. Stubbs
J. T. Cherry

Contents

NUCLEAR CRATERING ON A DIGITAL COMPUTER

Abstract

Computer programs based on the artificial viscosity method are applied to developing an understanding of the physics of cratering, with emphasis on cratering by nuclear explosives. Two established codes, SOC (spherical symmetry) and TENSOR (cylindrical symmetry), are used to illustrate the effects of variations in the material properties of various media on the cratering processes, namely shock, spall, and gas acceleration. Water content is found to be the most important material property, followed by strength, porosity, and compressibility.

Crater-profile calculations are presented for Pre-Gondola Charley (20-ton nitromethane detonation in shale) and Sedan (100-kt nuclear detonation in alluvium). Calculations also are presented for three 1-Mt yields in saturated Divide basalt and 1-Mt yield in dry Buckboard basalt to show crater geometry as a function of the burial depth for large explosive yields.

The calculations show, for megaton-level yields, that gas acceleration is the dominant mechanism in determining crater size and depends in turn on the water content in the medium.

Introduction

During the past decade, the concept of nuclear excavation has led to various engineering proposals, whose designs require a reliable procedure for determining the optimal explosive yields and depths of burial. The development of a reliable procedure requires at least

- An adequate understanding of the mechanisms of cratering with respect to variations in medium properties, yield, and depth of burial.
- A means of correlating and extending the field experience.

Cratering with nuclear explosives is essentially a wave propagation phenomenon. Computer programs based on the artificial viscosity method of calculating shock-wave propagation have had excellent success.[1-3] The first requirement for these calculations is a model of material behavior.

Cherry[4] developed a mathematical model for rock materials behavior and a corresponding measurement program, the results of which were included in the codes SOC (spherical symmetry) and TENSOR (cylindrical symmetry). The key to his success in calculating Scooter (0.5 kt HE in alluvium) and Danny Boy (0.42 kt NE in basalt) was recognizing that separate

descriptions were required of the material properties before and after failure. Since 1966, many equation-of-state measurements have been made on various types of rocks. The calculational model has been improved. This paper does not discuss in detail the calculational model (reports on the SOC and TENSOR codes are now being prepared) but does apply the codes to illustrate the state of the art—that is, our present understanding of cratering phenomena.

Mechanics of Cratering

In all wave-propagation problems, the boundary conditions determine the nature of the solution. In cratering, the principal boundaries are (1) the cavity formed by the explosion and (2) the ground surface. Both of these boundaries are free. The stress-wave interaction on these boundaries divides the process of crater formation into four observable, sequential phases: shock (compressive wave from cavity to ground surface), spall (rarefaction wave from ground surface to cavity), gas acceleration (recompaction wave toward ground surface), and ballistic trajectory (free fall).

Shock—The shock wave is a large stress discontinuity created when the restrained internal energy of a nuclear device is released. As the shock wave propagates in the medium, it compresses the rock, distributing internal and kinetic energy as it moves outward. The energy of the wave decays with distance from the source, and the state of rock changes in proportion to the energy deposited. Immediately around the source the rock is vaporized. This is followed by a region of melt. Crushed and fractured rock extends outward a considerable distance beyond the region of melt. The shock wave develops the conditions for formation of a large cavity around the source and imparts a momentum to the rock through which it travels.

Spall—A rarefaction wave is reflected when the shock wave reaches the free (ground) surface, relieving pressure in the rock as it travels back toward the cavity. Tension is developed in the rock, causing it to separate from the formation at a velocity characteristic of the momentum trapped in the rock. This increase in momentum establishes the conditions in the mound necessary for development of the gas acceleration phase. It also establishes the limits of the true crater above the shot point.

Gas Acceleration—Because rarefaction has relieved the pressures in the rock above the cavity (which still contains several hundred atmospheres of pressure), the resulting pressure differential accelerates the growth of the upper part of the cavity. Growth of the cavity may ultimately recompact the rarefied rock above it and additionally increase its momentum. The cavity expands rapidly toward the initial ground surface, forming the large observable mounds. Unrestrained spherical divergence of the mound leads to its disintegration, the horizontal component of velocity tending to drive the

sides of the mound away from the crater area.

Ballistic Trajectory (Free Fall)—On general mound disintegration, the final cavity pressure (1 or 2 atm) is vented. The forces of gravitation and friction alone now affect each particle that is on its own ballistic trajectory. The depth of the crater depends on the amount of fallback material and its bulking characteristics.

Figure 1 shows the effect of each mechanism on the particle velocity as a general function of time. The relative effect of each mechanism on the total mound velocity field depends on the material properties and defines the cratering characteristics of a medium. The mound velocity field at the end of the gas acceleration phase determines the crater geometry.

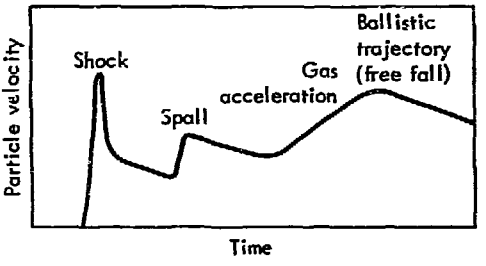

Fig. 1. Cratering mechanisms.

The Calculational Model

For predicting crater geometry without merely scaling from past explosions, a numerical technique has been developed which integrates the conservation laws of mass, momentum, and energy on a digital computer. This numerical technique replaces the continuous spatial distribution of stress, density, velocity, etc., with a set defined at discrete positions (zones) in the medium.

At any given time the stress, density, coordinates, and particle velocity of each zone is known. The conservation-of-momentum equation in differenced form provides a functional relationship between the applied stress field and the resulting acceleration of each point in the grid. Accelerations produce new velocities when allowed to act over a small time increment, Δt; velocities produce displacements, displacements produce strains, and strains produce a new stress field. Time is incremented by Δt, and the cycle is repeated.

The calculations are simplified when a degree of symmetry is specified. The SOC code integrates the conservation equations written in spherical symmetry (there is only a radial direction of motion permitted), while the TENSOR code allows study of cylindrically symmetric problems (such as craters) where two spatial variables must be considered.

The manner in which the strain is related to stress is called the equation of state of the material. This equation of state must describe the various modes of material behavior (gas, liquid, and solid) and allow for acceptable transitions among the modes. It must be determinable before the shot. Preshot logging and core tests have been used to satisfy this last requirement.

The preshot logging measurements are extremely important in determining the average properties of the entire rock structure and the layers of impedance

mismatch. These logs also are needed for proper selection of the core samples and verification that the tests are representative of the site.

Material Characteristics Important in Cratering

The equation of state (EOS) defines the cratering efficiency of a medium; that is, the equation of state specifies the amount of internal energy of the explosive which will be converted into kinetic energy in the mound above the explosive by shock, spall, and gas acceleration.

We have found the following four equation-of-state parameters important in determining cratering efficiency:

- Compressibility.
- Porosity (compactibility).
- Water content.
- Strength.

The first three relate to the hydrostatic loading and unloading characteristics of the medium. The fourth limits the permissible deviatoric stress in the rock.

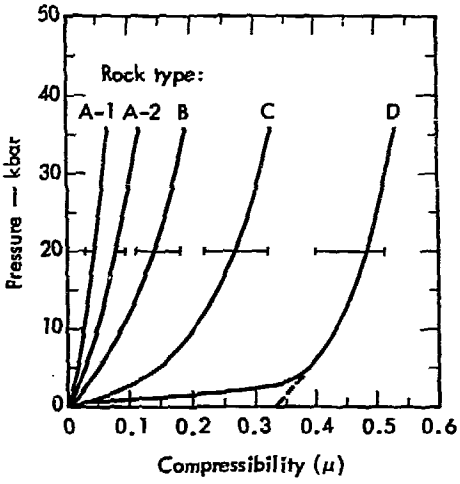

Fig. 2. Pressure-volume relationship for various rock types. [$\mu = (V_0/V) - 1$]

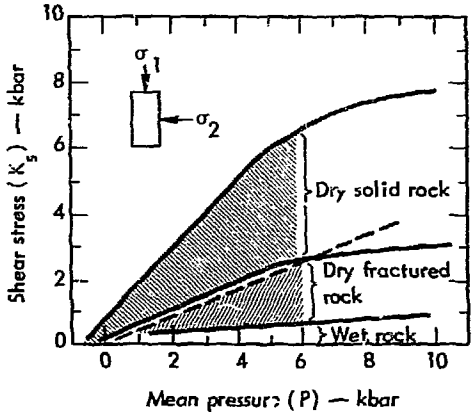

Fig. 3. Shear strength trends as a function of mean stress. [$K_S = (\sigma_1 - \sigma_2)/2$; $P = (\sigma_1 + 2\sigma_2)/3$]

Figure 2 compares the hydrostatic compressibility of the various types of rock listed in Table 1. The difference between hydrostatic loading and unloading in these types of rock is a measure of their nonrecoverable porosity. Table 1 gives the density, bulk modulus, and sound speed for the various rock types in their respective groupings.

Figure 3 shows the wide range of shear strengths vs pressure found among various rock samples in three general states: solid, fractured, and wet. Strength does not correlate as well with rock type (A-1, A-2, etc.) as it does with the state of the rock. The curves in this figure indicate a general trend in strength behavior; however, there are many exceptions to this idealized picture.[8]

Table 1. Significant parameters of various rock types.

Rock type	Rock and experiment	Density, g/cc	Sound speed, ft/sec	Bulk modulus, kbar	Ref.
A-1	Canal basalt	2.65	18,000	388	7
	Cabriolet (deep layer)	2.53	13,012	394	5
	Hardhat	2.65	18,000	552-333	5
	Buggy basalt (type 1)	2.60	9,000	480	6
	Buckboard basalt (type 1)	2.6	7,200	236	5
	Pre-Schooner VIT (type 2)	2.3	8,000	256	5
A-2	Palanquin type 1	2.5	7,961	149	5
	Palanquin type 2	2.4	5,000	116	5
	Cabriolet type 2	2.3	5,000	97	5
	Faultless tuff	2.283	11,500	160	6
B	Bear Paw (Fort Peck) shale	2.2	6,000	50.5	6
	Buggy basalt (type 3)	2.38	5,000	77	6
	Greeley tuff	2.0	10,150	47.5	6
	Gas Buggy sandstone	2.48	13,500	100	6
C	Cabriolet (type 3)	1.98	3,600	13.5	5
	Palanquin (type 3)	2.0	2,975	19.4	5
D	Buggy basalt (type 5)	1.94	3,600	18	6
	Alluvium	1.5	3,000	18	5
	Scroll	1.4	4,200	19-28	6

The effect of material properties on the cratering mechanism can be illustrated readily by a parameter study on SOC.

COMPRESSIBILITY AND POROSITY

Figure 4 is a plot of the peak shock stress vs distance as calculated by SOC, illustrating the effect of compressibility and porosity on shock-wave attenuation. It can be seen that peak pressures are attenuated more rapidly for the more compressible rock. If additionally, the rock is compactible (porous), peak pressures are further attenuated. Figure 5 is the particle velocity corresponding with Fig. 4 at a specific time. (For the corresponding equation of state, see Fig. 2.) The peak particle velocity of the shock front is proportional to the shock stress and thus is controlled by the stress attenuation. It is interesting to note that the velocity field in the mound behind the shock varies slightly with compressibility and porosity.

STRENGTH

The behavior of the shock wave due to shear-stress variations is not a simple function of the shear strength but depends on the entire equation of state. Naturally, the higher the shear stresses allowed to develop, the more severe is the attenuation.

An interesting parameter study is the effect of the fractured strength of the rock on the particle velocity of the entire mound. Figure 6 shows the decay of particle velocity behind the shock wave as the fractured strength is increased from 0-0.5 kb to 5.0 kb. The fractured rock strength is one of the primary equation-of-state

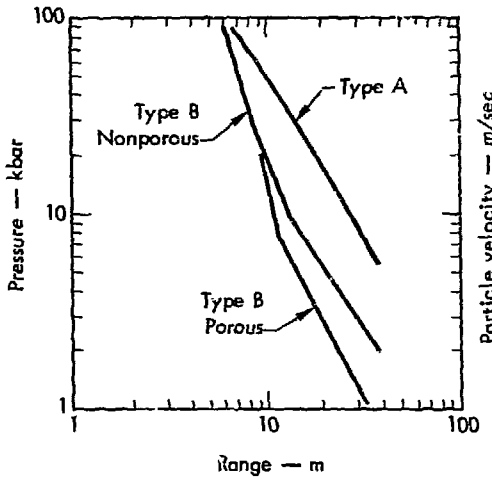

Fig. 4. Shock attenuation as a function of compressibility and porosity.

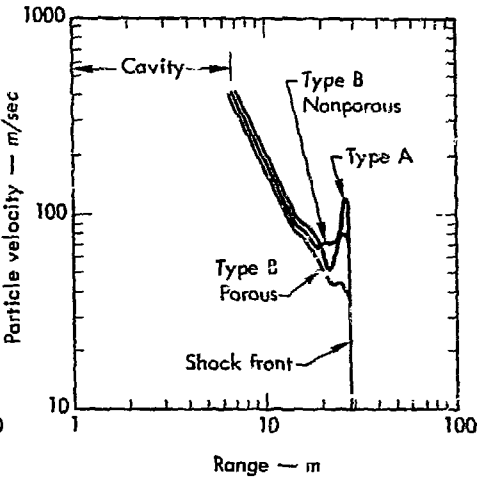

Fig. 5. Particle velocity as a function of compressibility and porosity.

parameters determining the cratering efficiency of the rock.

A recent study in saturated quartz rock illustrates the sensitivity of the rock strength on the cratering efficiency, for burst depths greater than optimum. Strength data from the core tests indicate two distinct strength behavior characteristics,[9] as shown at the top of Fig. 7. To assess the effect of strength variations on the mound velocity field, two SOC calculations were made at 175 kt, using strength curves A and B. The yield was increased to 225 kt and a new calculation run with Curve A. Figure 7 (lower) shows that the reduction in strength results in the same mound velocity as a 25% increase in yield at the higher strength.

At optimum depth of burst or shallower depths, such a variation in strength is of little consequence in determining the crater radius; however, for greater depths, strength variations play a dominant role in determining the crater size.

WATER CONTENT

Static tests have demonstrated that the presence of free water within a rock significantly reduces both its nonrecoverable porosity and the ultimate shear strength of the sample (Fig. 3). As indicated earlier, reducing either of these parameters leads to an increase in the cratering efficiency of the medium. Also, vaporization of free water in the rock by the shock wave, outside the initial radius of rock vaporization, creates a larger source region, of which a significant fraction is noncondensable water vapor.

The effect of the larger source region, maintaining higher pressures than dry rock, is about a 10% increase in spall velocities. More significantly, this provides a strong, long-lasting, gas acceleration phase.

Because there is a lack of experimental data on the release paths of a rock-water system, a simple approximation is made

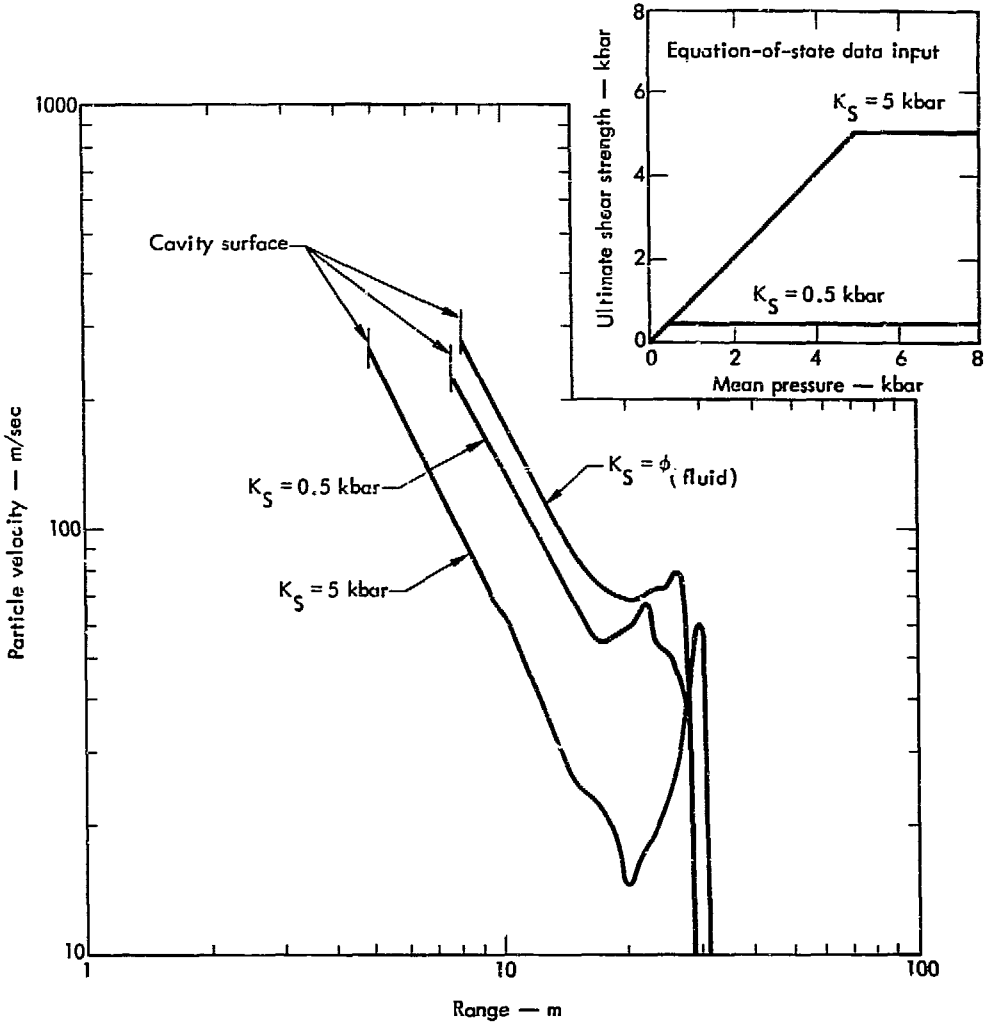

Fig. 6. Particle velocity as a function of shear strength. [$K_S = (\sigma_1 - \sigma_2)/2$; $P = (\sigma_1 + 2\sigma_2)/3$]. (a) Shear strength as a function of mean stress. [$K_S = (\sigma_1 - \sigma_2)/2$; $P = (\sigma_1 + 2\sigma_2)/3$].

in the calculational model to simulate this effect.

Piork et al.[10] developed an equation of state of water which gives the isentrope release paths from various shock states on the Hugoniot. The slopes of the isentrope, in general, vary from 1 to 2 in the log P-log V plane for pressures exceeding 150 kbar. The calculational model approximates this behavior for a rock-water system using

$$P = P_H + \frac{\Gamma}{V}(E - E_H),$$

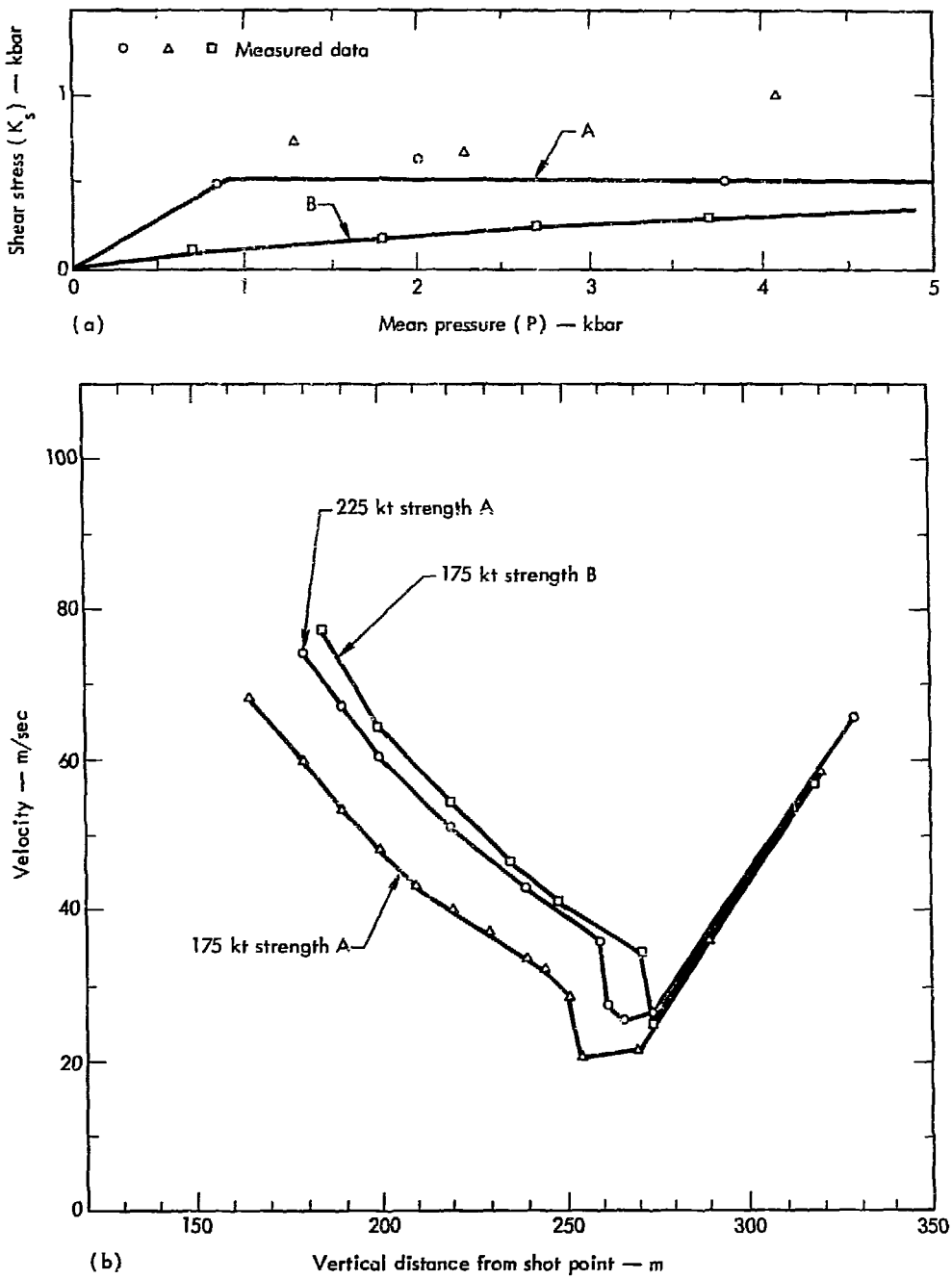

Fig. 7. Particle velocity as a function of shear strength and yield in saturated quartz.

where

P is the pressure,

E is the energy,

V is the specific volume,

Γ is the Grüneisen gamma,

and subscript H refers to the Hugoniot values at a given specific volume. We further assume that

$\Gamma = 1$ for $P > 400$ kbar

$\phi < \Gamma < 1$ for 400 kbar $> P >$ 100 kbar

$\Gamma = \phi$ for $P <$ 100 kbar.

Calculations using the Grüneisen gamma approximation behave in a manner similar to calculations with nitromethane. Nitromethane has a Chapman-Jouguet pressure of 143 kbar, and the cavity radius scales as 5.5 m/(kt)$^{1/3}$. For a nuclear shot in a dense medium, the radius at which the shock stress falls below 150 kbar scales as approximately 5.1 m/(kt)$^{1/3}$.

CRATERING EFFICIENCY

We have defined the cratering efficiency of the medium in terms of the kinetic energy developed in the mound by the explosive. The efficiency is determined in turn by the equation of state of the rock. To illustrate these relationship, mound velocity profiles were calculated on SOC for three media in which there is cratering experience. The first medium was Bear Paw shale from the Fort Peck reservoir: saturated, nonporous, and extremely weak. The second was Sedan alluvium: very porous, moderately weak, and wet (10% water at the depth of the calculation). The third was NTS Buckboard basalt: dry, porous, and moderately strong.

Figure 8 shows the velocity profiles between cavity and free surface for the three media. These calculations were for

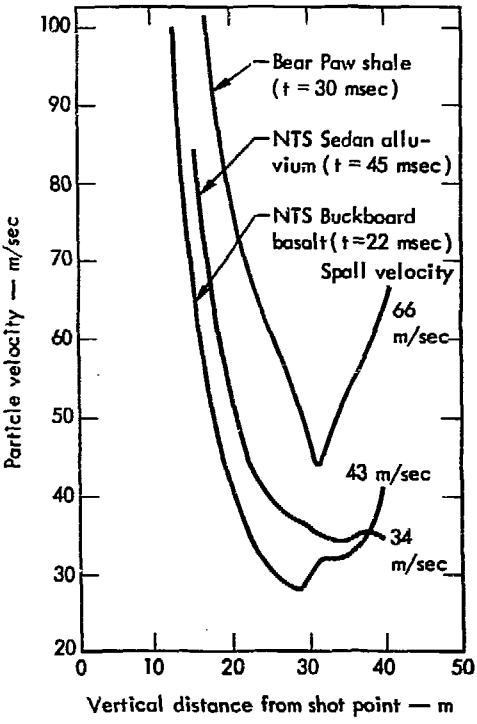

Fig. 8. Mound velocity field for three cratering media where t = time of arrival of rarefaction wave at cavity surface.

a 1-kt nuclear yield at a depth of 40 m. The plots were taken at the moment the rarefaction wave arrives at the cavity, which varies because of differences in the compressional wave velocity for the medium. Figure 9 shows empirical, scaled cratering curves for the three media. Comparing the velocity curves with the cratering curves shows a definite correlation between the velocity field behind the spalled region and the crater radius.

In summary on this section — compressibility and porosity of the rock are the dominant factors in determining the energy delivered to a point in that medium. However, the shear stress and

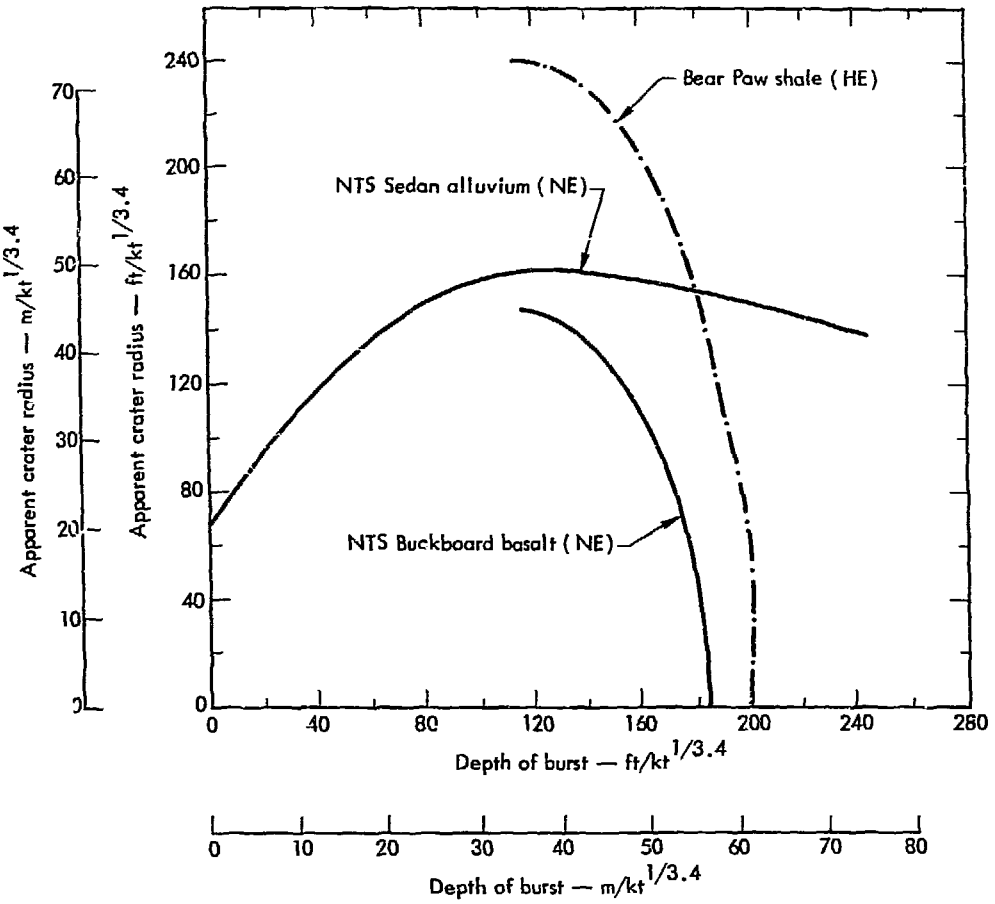

Fig. 9. Scaled crater radius curves.

length of time that the stress operates primarily determine the velocity field behind the shock or the spalled region. The final velocity field through the mound then depends on the effectiveness of the gas acceleration phase.

If the material properties were listed in order of importance for determining the cratering efficiency of the medium, the list should be:

1. Water content.
2. Shear strength.
3. Porosity.
4. Compressibility.

The water content is of primary importance because it decreases the rock compressibility and porosity and drastically reduces its shear strength. Water content also provides an additional energy source in expansion of the noncondensable water vapor. All of the above factors increase the velocity field of the mound and therefore the cratering efficiency of the medium.

Cratering Calculations

Once the site, yield, and approximate depth of burial of a proposed cratering experiment are determined, the hole is drilled, and in situ velocity and density logs are run. From the density, compression, and shear velocity logs, core samples are selected for high-pressure testing, mineralogy, porosity, and water-content measurements. High-pressure testing consists of (1) hydrostatic compressibility measurements, both loading and unloading, up to 40 kbar, (2) Hugoniot (150-700 kbar) data, and Hugoniot elastic limit if measurable, and (3) shear strength for confining pressures up to 10 kbar.

A best fit for Poisson's ratio is determined from the in situ logging data and the initial bulk modulus as determined from the hydrostatic compressibility measurements.

With the completion of the equation of state, a SOC calculation is made to determine the radius of vaporization, develop the gas tables for the vaporized rock, and check the EOS for errors. A TENSOR grid is established whereby the energy of the device is distributed uniformly throughout the cavity. The problem is monitored until the shock, spall, and gas acceleration phases are completed and/or large pressure or velocity gradients are no longer present in the mound. At this time, a free-fall throwout calculation is performed. The throwout calculation consists of removing from the grid and stacking on the ground surface those zones which are calculated to have sufficient velocity to clear the free surface. The ballistic trajectory of these zones determines their final position on the surface. Mass is conserved during the entire calculation.

The crater radius is determined by the location of the ejecta as calculated by the throwout code. Determination of the crater depth, however, is not direct calculation. The lower hemisphere of the cavity never reaches equilibrium in the TENSOR calculations. Also, overburden is neglected in the TENSOR code. The final position of the lower hemisphere of the cavity is determined by an averaging process involving spherical calculations with SOC (which considers overburden) and the existing velocity and pressure field around the cavity in TENSOR at the time of the throwout calculation.

In all calculations carried past 2 sec, the pressure gradient outside the lower cavity surface has reversed the velocity field of the material around the lower hemisphere.

This series of cratering calculations has resulted from a feasibility study on the proposal for a nuclear isthmus canal. The canal rock is saturated; unfortunately, cratering experiments in saturated media are limited to chemical explosives. The Pre-Gondola series (20 tons of nitromethane at various burst depths) provides a test of the codes in saturated media with material properties at low pressures. Sedan, a 100-kt nuclear burst in alluvium with 10-20% water content, provides a test of the vaporized water expansion approximation.

PRE-GONDOLA SHALE

The compressibility curve for Pre-Gondola shale is the type B curve in Fig. 2.

The phase change of water reported by Stephens[6] at 10 and 22 kbar has been smoothed out. The unconfined shear-strength tests varied considerably but were consistent with 11 bars of residual strength after 2-3% strain. Figure 10 is a plot of the yield surface used in the calculation to represent this type of behavior (Bear Paw shale). Figure 11 compares the measured radial stress at three gages with the SOC calculation for Pre-Gondola Bravo.[11] Figure 12 plots peak radial stress and velocity for Bear Paw shale, comparing measurements with the SOC calculation.

Figures 13 and 14 deal with Pre-Gondola Charley, one of a series of nitromethane cratering shots conducted by the U.S. Army Engineers Nuclear Cratering Group at LRL to determine the cratering curve for Bear Paw shale. Pre-Gondola Charley was a 20-ton burst at 42.5 ft. Figure 13 shows the peak velocity at various points on the mound surface as measured and calculated by TENSOR. Figure 14 is the resulting crater with throwout calculation.

Agreement among the stress wave form and peak particle velocity measurements is excellent. The surface velocities calculated by TENSOR also agree well with the surface motion measurements at various distances from ground zero.

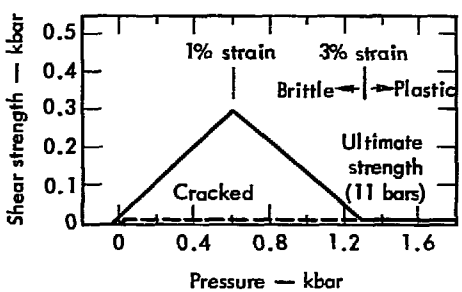

Fig. 10. Shear strength for Bear Paw shale at Fort Peck reservoir.

The throwout calculation at 107 msec yielded a slightly larger crater than measured, with very little fallback. This is not surprising in that the material in the mound around the cavity was compressed at 107 msec, and expansion of the rock to its original density or bulking was not taken into account.

SEDAN

Sedan was a 100-kt nuclear cratering event buried at 635 ft in fairly competent alluvium. The water content at the Sedan site varies from about 10% in the first 30 m to about 20% at a depth of 300 m.[12]

Compressibility curve type D (Fig. 2) was used for the calculation. The ultimate shear strength had to be estimated (Fig. 15) because no experimental shear-strength data exist. The material was assumed to behave ductilely above 0.4 kbar, and a constant Poisson's ratio of 0.33 was used. The density varied at the site with depth from 1.6 to 1.8 g/cc, with corresponding sound velocities of 3000 to 5000 ft/sec. For the calculation, a density of 1.7 g/cc and compressional velocity of 4000 ft/sec were used.

Figure 16 compares the measured surface velocity for Sedan near ground zero with the velocity as calculated by TENSOR. The calculation of the spall velocity proved slightly high, and the arrival of the recompaction front was later than calculated, but the calculation-measurement agreement of peak velocity at the end of the gas acceleration phase was excellent.

Figure 17 shows the Sedan crater profiled from the throwout calculation, which

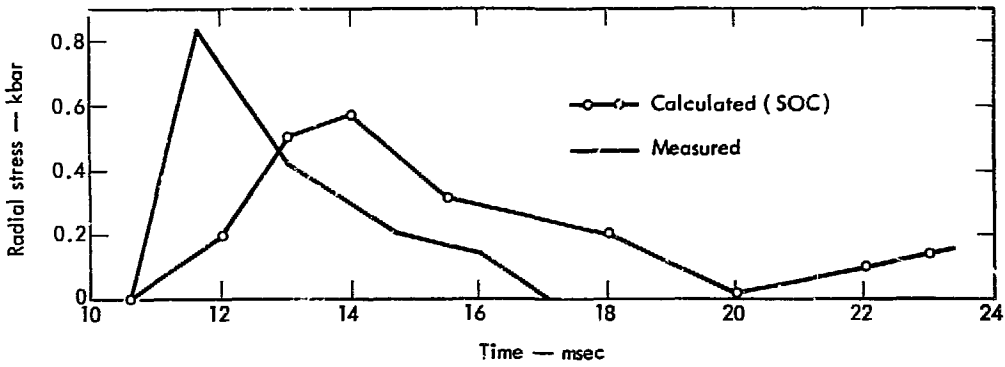

(a) Gage 2-o-2 (85-ft range)

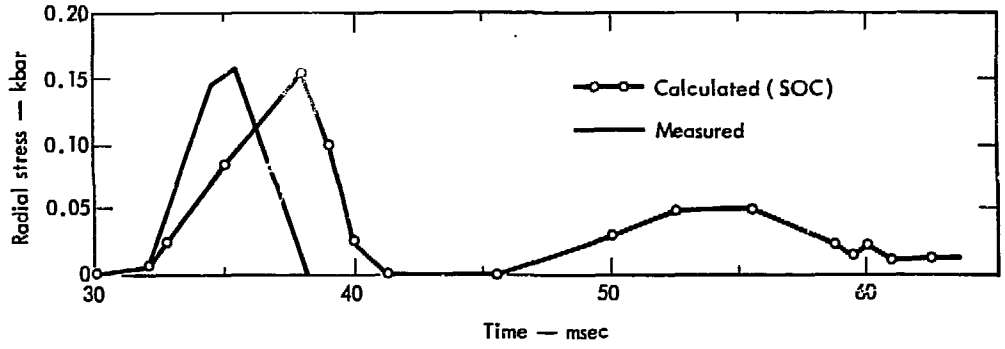

(b) Gage 22-o-9 (225-ft range)

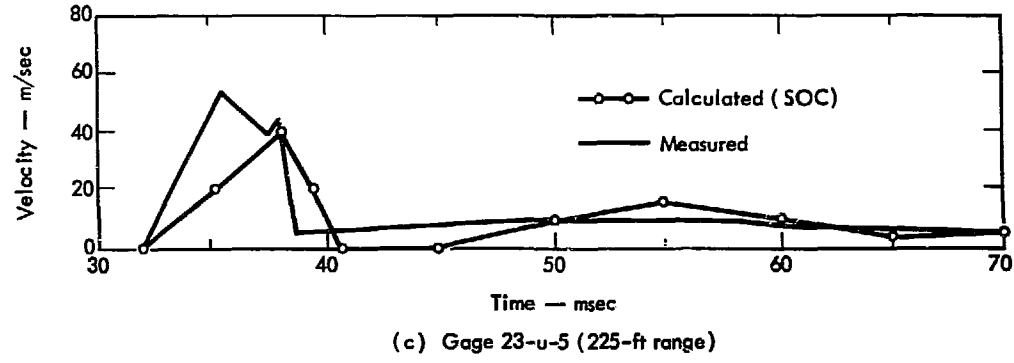

(c) Gage 23-u-5 (225-ft range)

Fig. 11. Measured and calculated stress history for Pre-Gondola Bravo.

agrees well with the observed crater profile. Calculation of the cavity rebound agrees fairly well with the measured lower hemisphere of the cavity. Ejecta that did not clear the crater filled this volume for the correct depth.

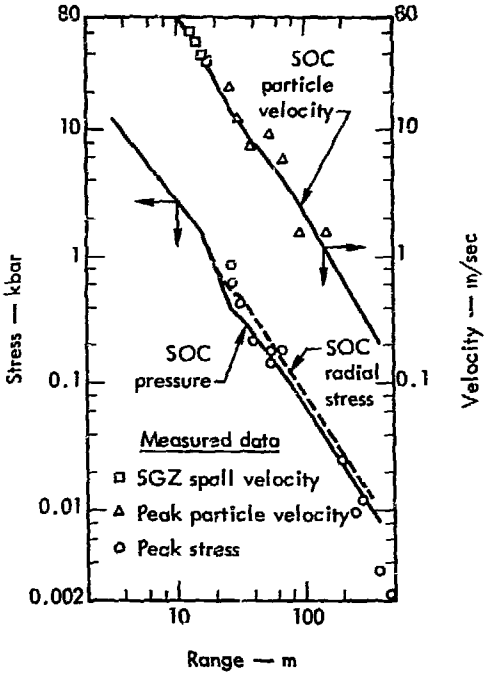

Fig. 12. Peak stress and particle velocity vs range, Pre-Gondola Bravo.

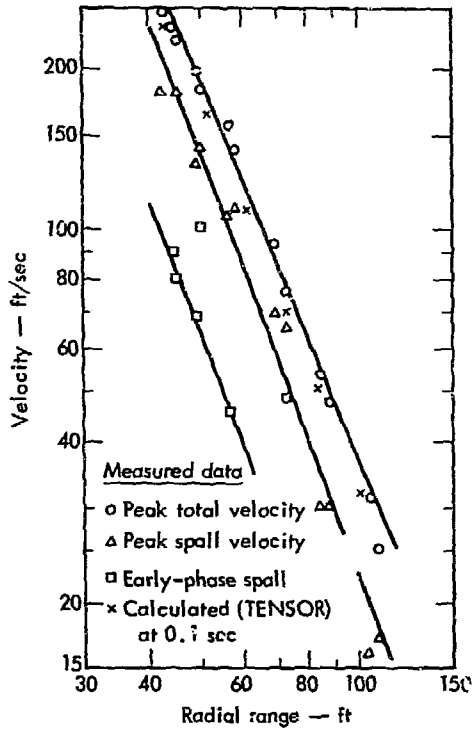

Fig. 13. Surface velocities vs radial range, Pre-Gondola Charley.

The results of this calculation suggest that approximations made on the expansion behavior of water vapor are within reason and compatible with our experience and knowledge to date.

BUCKBOARD BASALT

The Basalt type chosen for calculation was characteristic of the Danny Boy site on Buckboard Mesa, NTS. The site is moderately fractured, with open fractures randomly oriented at a frequency of 5-10 ft. The density is 2.62 g/cc with a compressibility-wave velocity of 7200 ft/sec. Figure 18 is the assumed strength curve, and Fig. 19 shows compressibility-curve loading and unloading as measured

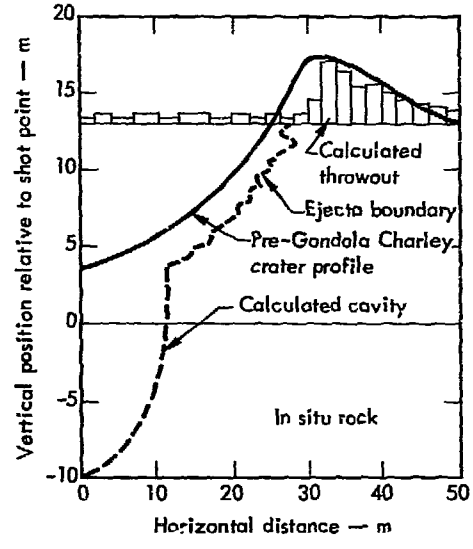

Fig. 14. Calculated crater profile for Pre-Gondola Charley.

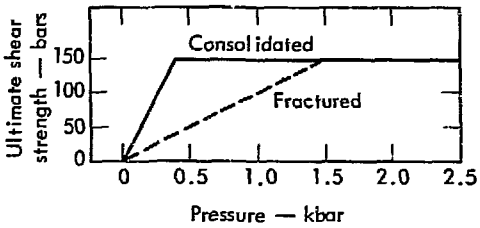

Fig. 15. Strength curve for Sedan crater calculation.

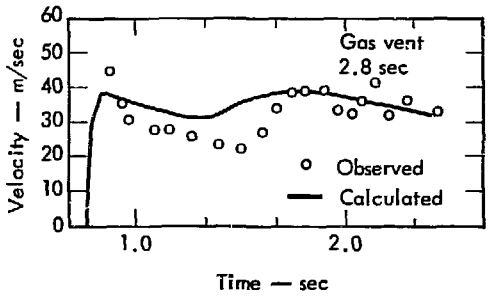

Fig. 16. Calculated and observed ground-zero surface velocity for Sedan.

by Stephens et al.[5] Strength measurements were not available. A constant Poisson's ratio of 0.33 was used.

Data on the Danny Boy Event (0.42 kt NE at a depth of 33 m), previously published by Cherry,[4] were recalculated to check changes in the TENSOR code.

Figure 20 shows the crater as calculated, in excellent agreement with the experimental result..

Next, a 1-Mt calculation at 328 m was performed to investigate the cratering efficiency of the basalt at high yields. The identical equation of state was used in the calculation as for Danny Boy. Figure 21 shows the crater profile as calculated. A large portion of the ejecta remained in the crater area, with the resulting apparent crater due to compaction of the medium.

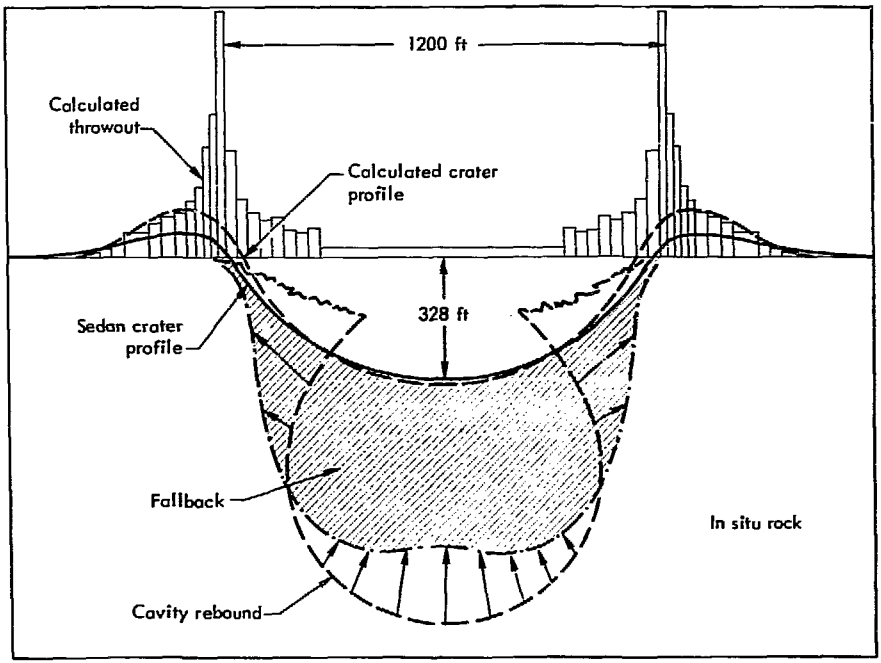

Fig. 17. Sedan crater profile at t = 2.4 sec.

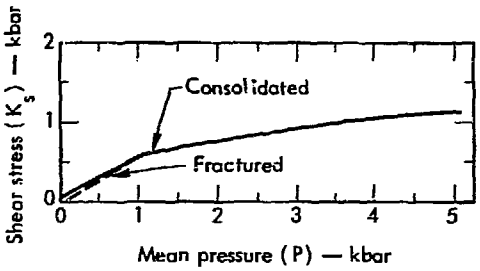

Fig. 18. Strength curve for Buckboard basalt. [$K_S = (\sigma_1 - \sigma_2)/2$; $P = (\sigma_1 + 2\sigma_2)/3$].

A 10% bulking factor was used for the fallback. With $W^{1/3.4}$ scaling, the megaton calculation was at the same scaled burst depth as Danny Boy. However, while the Danny Boy crater was nearly optimum in size, the megaton burst barely produced a crater. In fact, the crater as shown in Fig. 21 appears deeper than that which would be actually realized; the calculation was terminated before the rebound of the lower hemisphere developed.

CALCULATIONS FOR AN ISTHMUS CANAL

One of the major problems in designing an isthmus canal is the need to crater a sea-level channel through the Continental

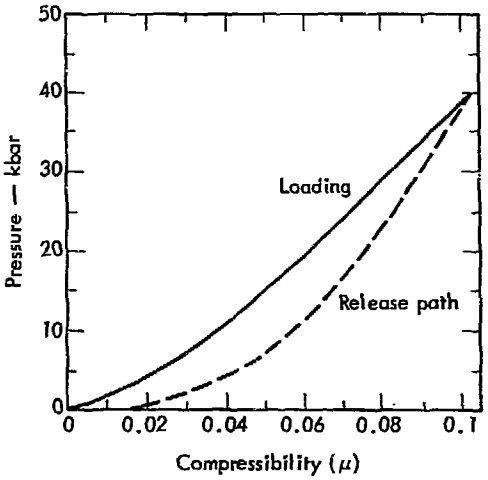

Fig. 19. Compressibility curves for Buckboard basalt. [$\mu = (V_0/V) - 1$].

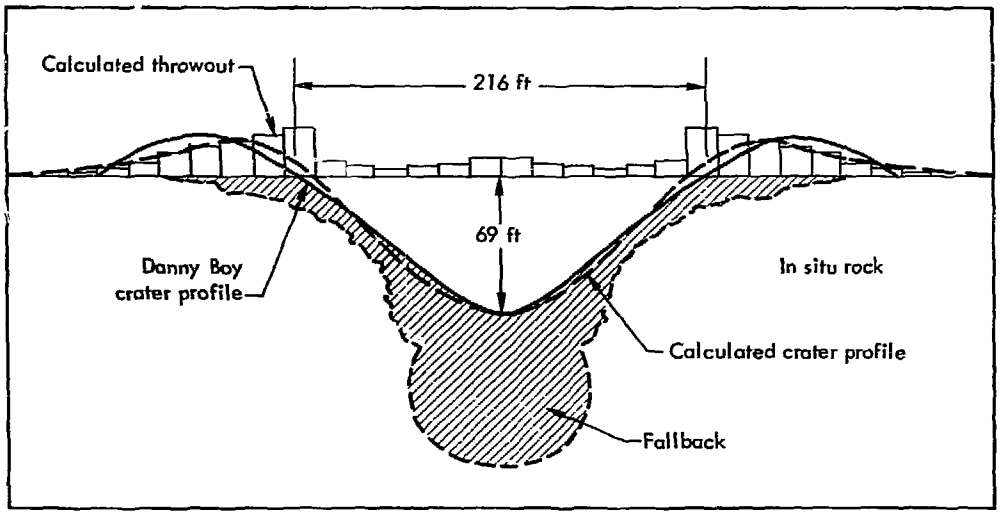

Fig. 20. Calculated crater profile for Danny Boy at t = 0.1 sec.

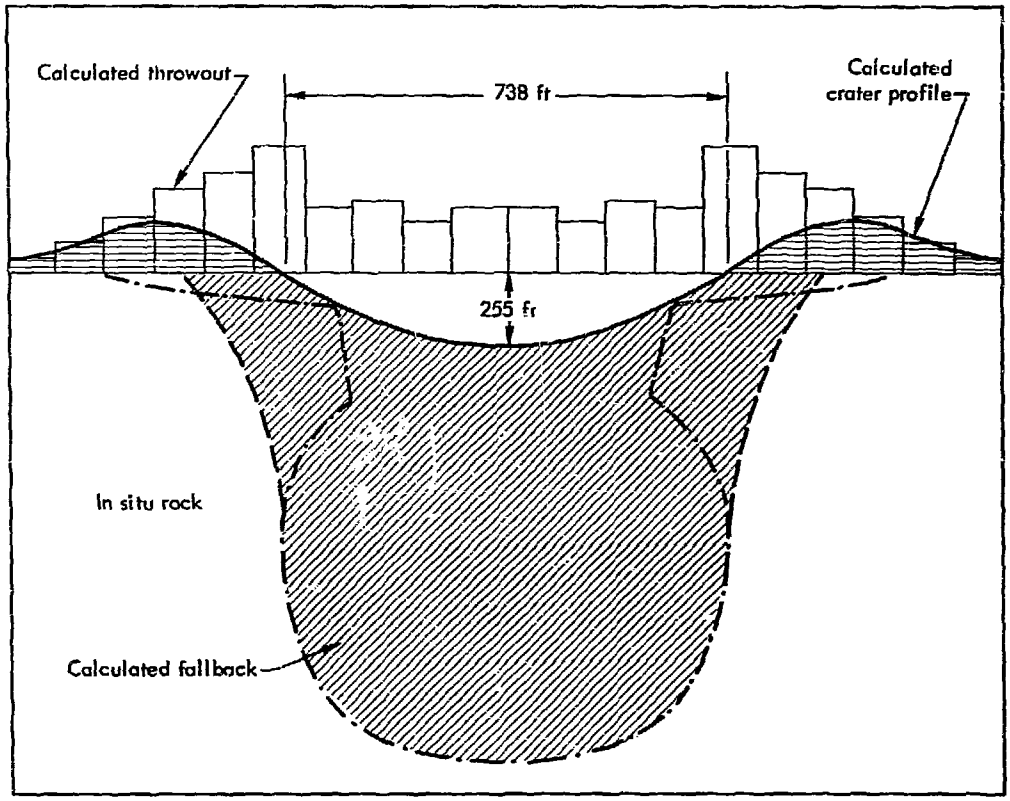

Fig. 21. Calculated crater profile for 1-Mt yield in Buckboard basalt, 328 m, at t = 1.5 sec.

Divide. For Route 17, the most prevalent rock types in the region of the Continental Divide are the basement-complex basalt, tuff agglomerate, and Morti tuff.

Figure 22 shows the equation-of-state data—Hugoniot, compressibility, and strength—for all rock types tested on Route 17.

Figure 23 shows the equation-of-state data for Route 25. A comparison of Fig. 22 with Fig. 23 indicates that the behavior of the rocks under testing for the two routes is almost identical, and the differences between the basalt and tuff agglomerate are so slight that only one of the rocks needs to be studied in detail. A comparison of the canal equation-of-state data (Figs. 22, 23) with equation-of-state data from other cratering shots (Figs. 2, 3) further emphasizes the very small variation in material properties between the two routes.

Therefore, for the purposes of the feasibility calculations, the basalt from 17-11 was chosen as the primary divide rock (Rock type A, Fig. 2), and a single calculation was done for the Morti tuff [17-15] (Rock Type B).

The strength of the rock as function of pressure is shown in Fig. 24.[13] The

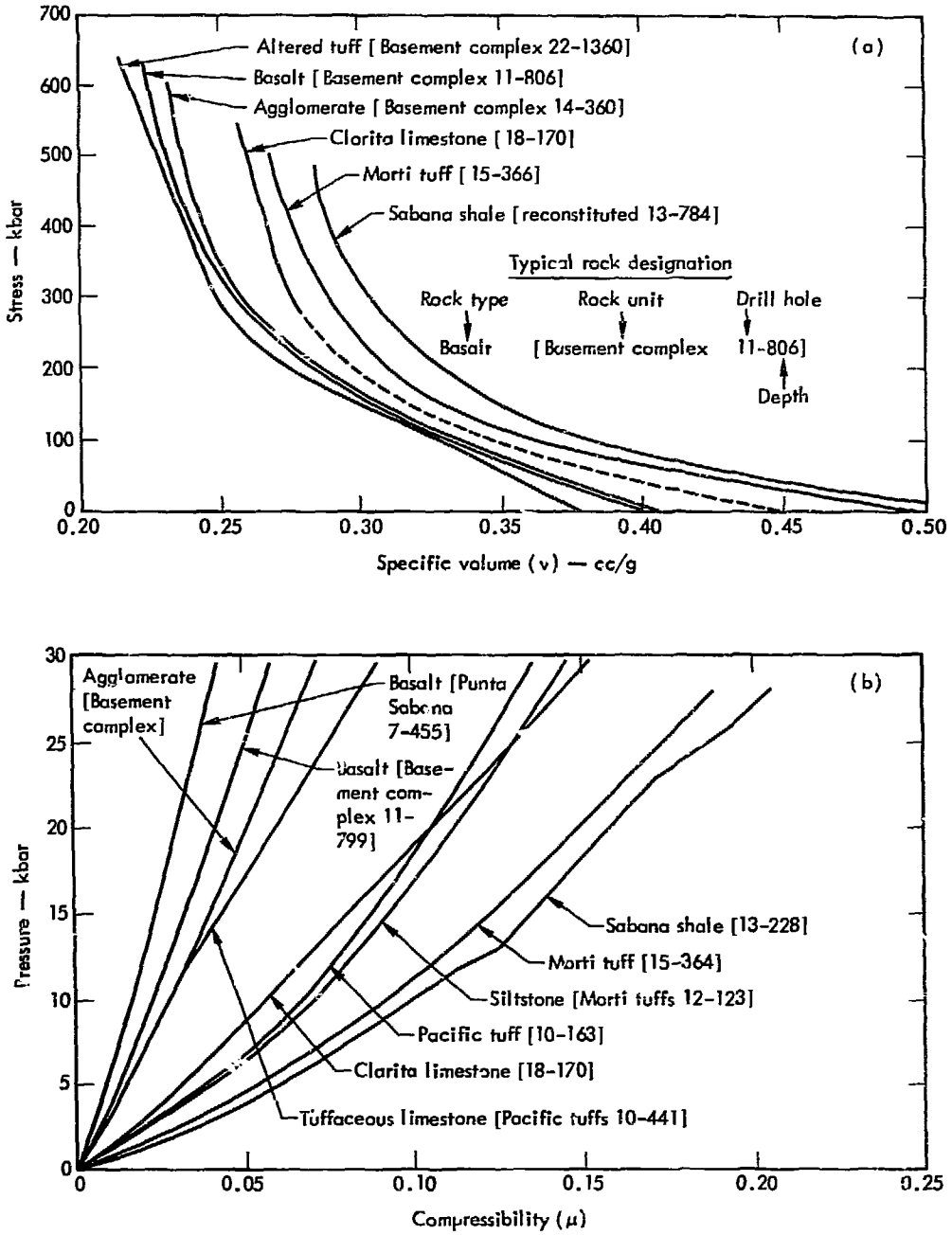

Fig. 22. Equation-of-state data, Route 17. (a) Hugoniot, (b) compressibility, and (c) strength.

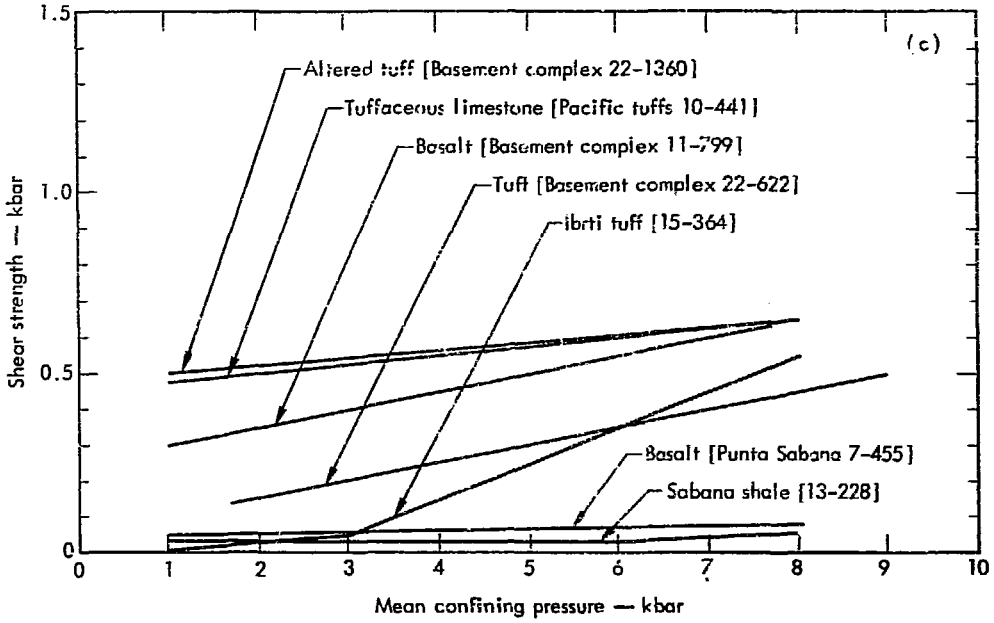

Fig. 22 (Cont'd.)

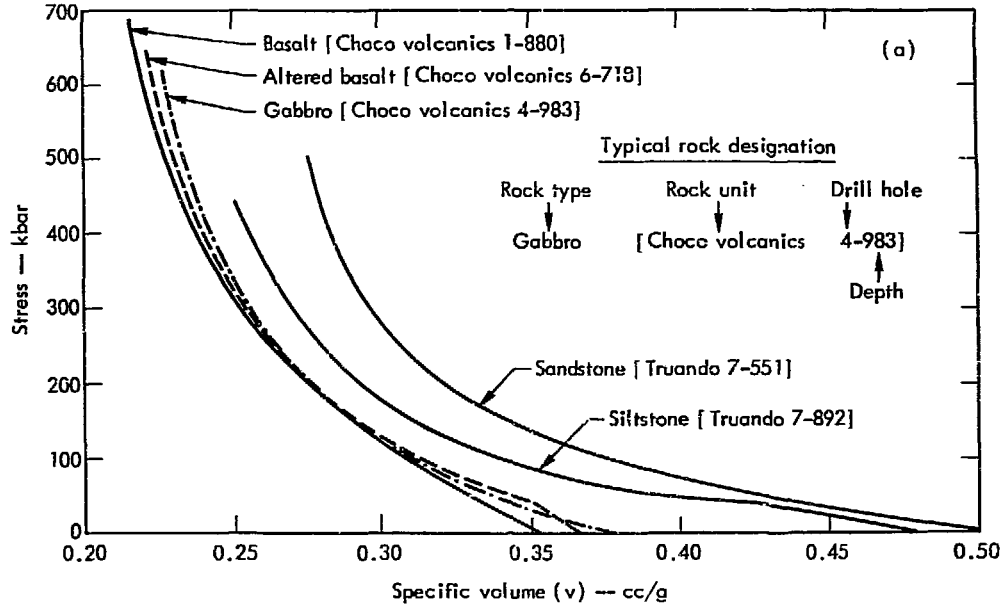

Fig. 23. Equation-of-state data, Route 25. (a) Hugoniot, (b) compressibility, and (c) strength.

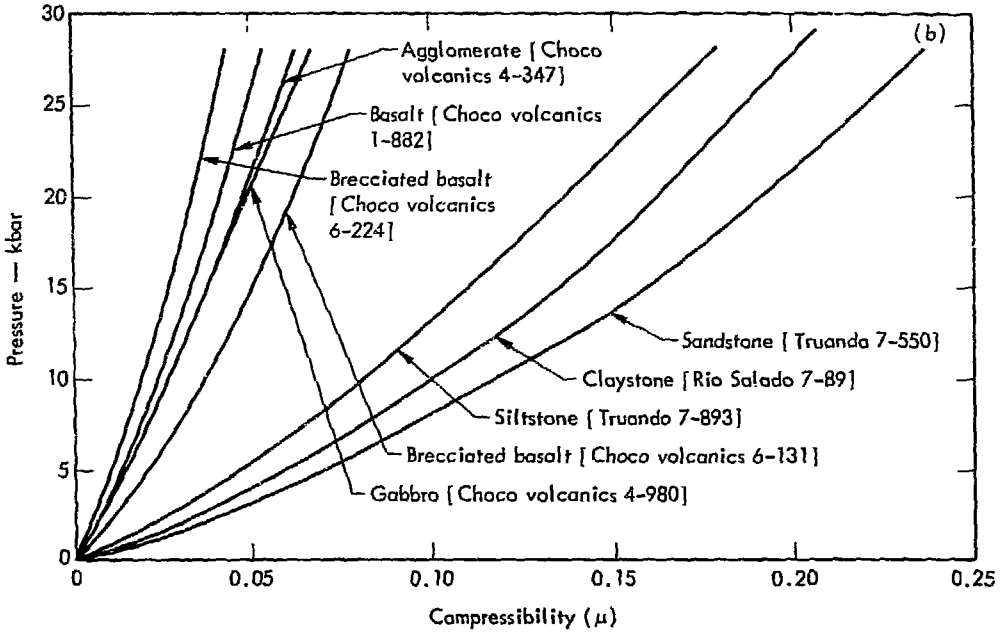

Fig. 23 (Cont'd.)

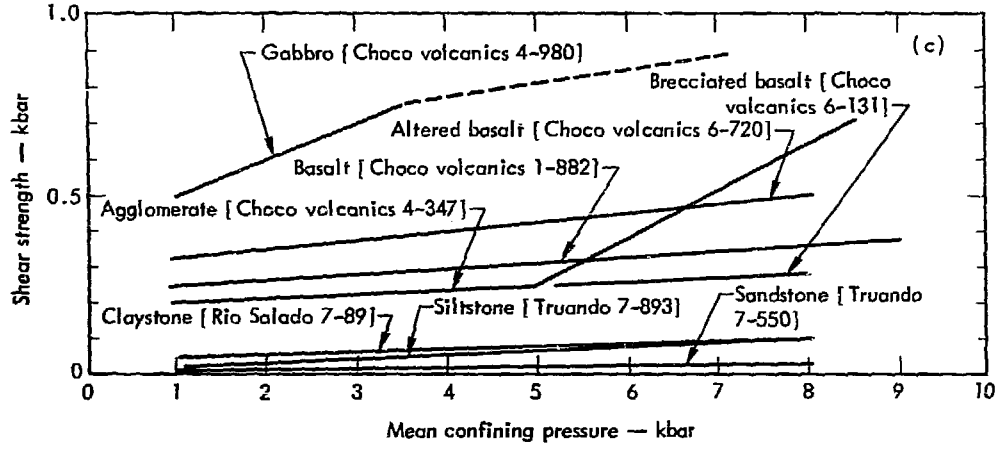

Fig. 23 (Cont'd.)

brittle-ductile transition point is 0.5 kbar, and a Poisson's ratio of 0.3 was used in the calculations. The initial density was 2.65 g/cc. .

To develop a correlation on the cratering efficiency of the Canal basalt, a calculation was made based on the Danny Boy yield and depth of burial (0.42 kt at 33 m).

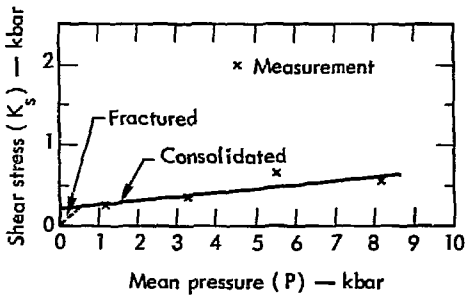

Fig. 24. Shear strength for Divide basalt. [$K_S = (\sigma_1 - \sigma_2)/2$; $P = (\sigma_1 + 2\sigma_2)/3$].

Figure 25 compares the calculated Canal basalt crater with the measured crater from Danny Boy. At this yield and depth of burst, the Canal basalt is about 25% more efficient as a cratering medium than Buckboard basalt. Spalling was the dominant cratering mechanism.

Figures 26 through 28 show 1-Mt crater calculations at burst depths of 139, 328, and 400 m, respectively, in Canal basalt.

At a depth of 139 m, a megaton crater is completely due to spalling. This problem was terminated at 200 msec, at which time the average mound velocity was 400 m/sec. The calculated crater may be slightly larger than that which would actually result, due to neglect of shear forces at the crater edges in the throwout calculation.

At 328 m, a strong gas acceleration developed to enhance the dimensions of the crater. At 463 msec, when the existing velocity was primarily due to shock and spall, a throwout calculation gave an apparent crater radius of 260 m (855 ft) and depth of 170 m (560 ft). At 4.0 sec the gas acceleration phase was complete; the throwout calculation gave an apparent crater radius of 390 m (1280 ft) and depth of 228 m (748 ft).

At 400 m, gas acceleration was needed to form a crater. Even with gas acceleration, a considerable amount of the ejecta

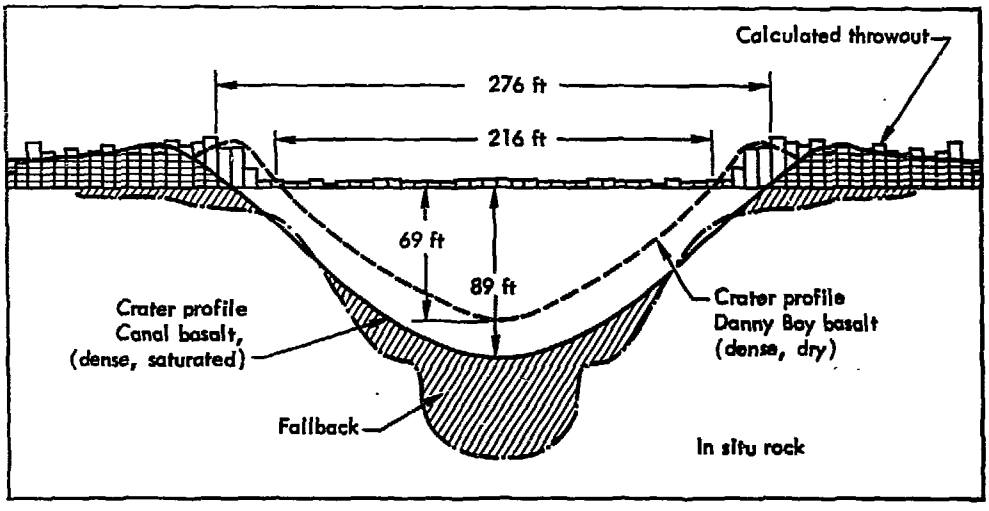

Fig. 25 Calculated crater profile for 0.42-kt yield in Divide basalt, 33 m, at t = 100 msec.

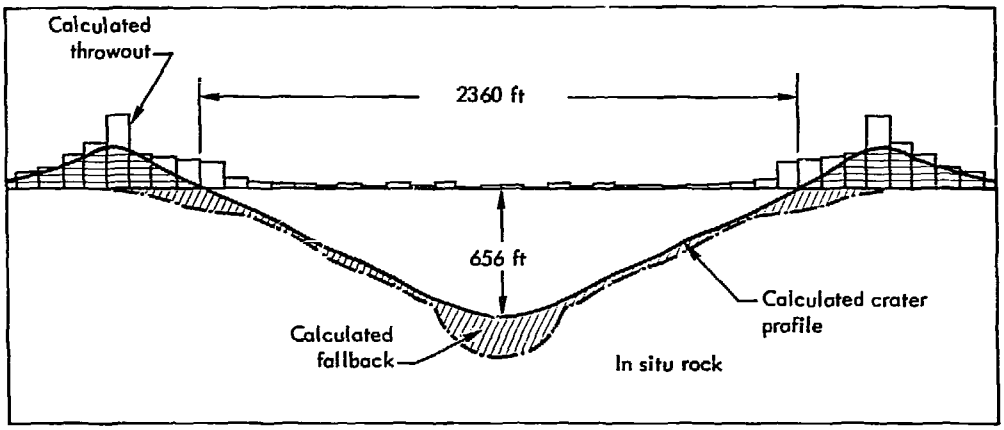

Fig. 26. Calculated crater profile for 1-Mt yield in Divide basalt, 139 m, at t = 200 msec.

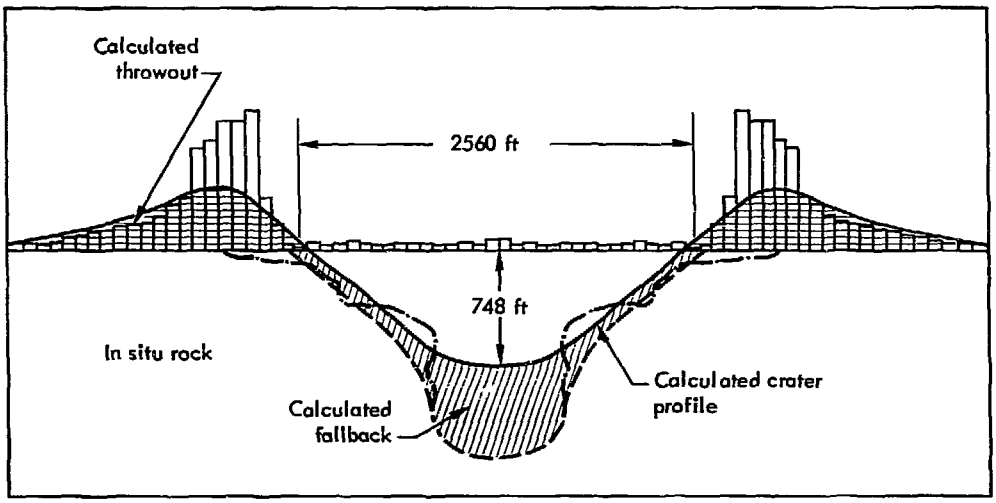

Fig. 27. Calculated crater profile for 1-Mt yield in Divide basalt, 328 m, at t = 3.0 sec.

was calculated not to clear the cratering area.

The compressibility and strength data used for the Morti tuff calculations are shown in Fig. 22, labeled Morti tuff [15-364]. The density used was 2.043 g/cc. The rock was treated as ductile with a Poisson's ratio of 0.33. A strain-rate effect was introduced to allow a maximum shear stress of 1 kbar for high strain rates.

Figure 29 shows the calculated crater profile for 1 Mt at a depth of burial of 328 m in Morti tuff.

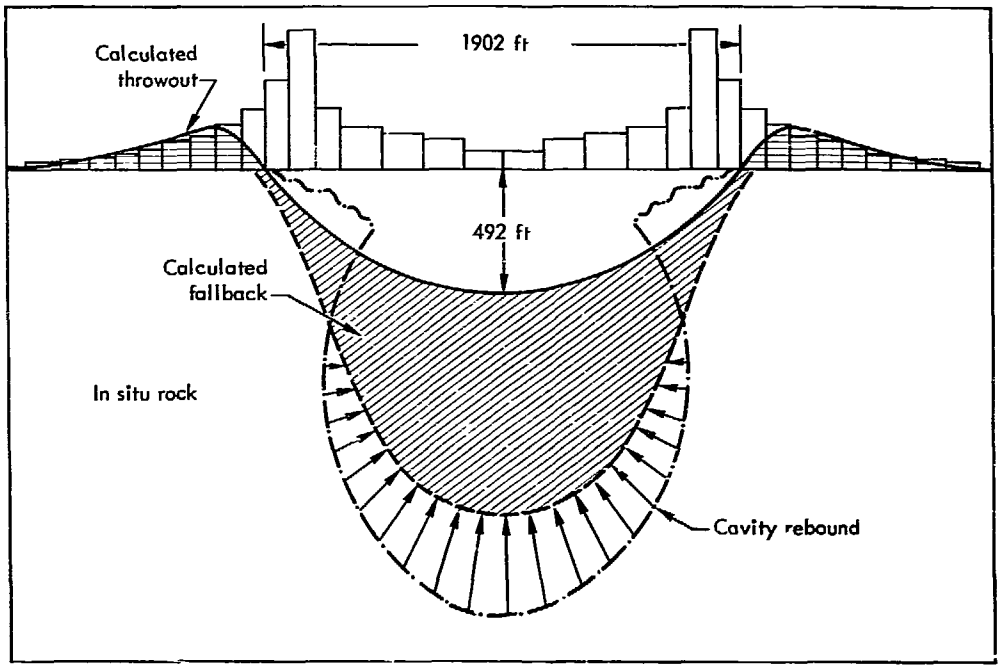

Fig. 28. Calculated crater profile for 1-Mt yield in Divide basalt, 400 m, at t = 4.0 sec.

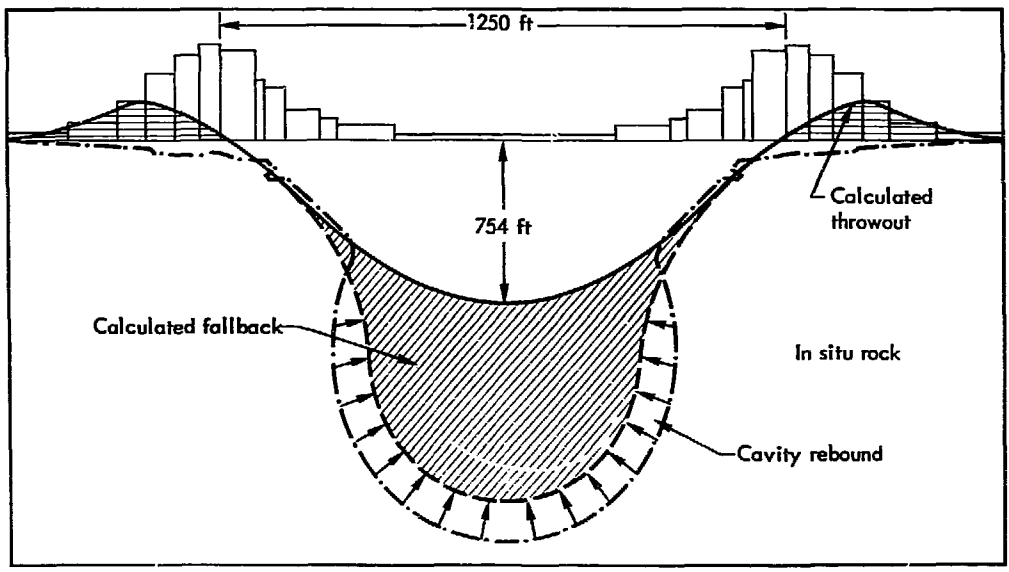

Fig. 29. 1-Mt crater in Morti tuff.

The Morti tuff was more compressible than the Divide basalt, but this was compensated for by the lower strength; thus the crater formation and size for the Morti tuff was almost identical with the Divide basalt at the megaton yield.

SPALL VELOCITIES

Figure 30 shows the calculated spall velocities, scaled for depth of burial for the Divide basalt and tuff, as compared with those calculated for Buckboard basalt and NTS alluvium.

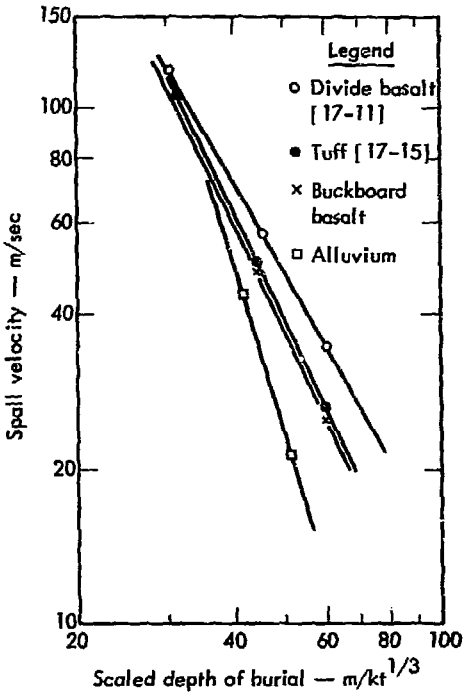

Fig. 30. Spall velocity as a function of scaled depth of burial.

Scaled Cratering Curves

Nordyke developed an empirical scaling law for apparent crater radius and depth vs depth of burst. According to this law, the scaled length is length divided by the yield in kilotons to the 1/3.4 power.

Figures 31 and 32 show crater calculations with the scaled curves for crater radius and depth, respectively. Comparing the curve for Buckboard basalt at about 0.5 kt with the megaton calculation in Buckboard basalt shows considerable yield effect. The optimal depth of burial is much shallower (scalewise) for a megaton yield than for a yield of about 0.5 kt. The reason for this is that dry Buckboard basalt does not develop a strong gas acceleration phase due to lack of noncondensable products in the cavity gas. Thus gravity dominates in controlling the velocity field for much of the characteristic time of event, resulting in craters that scale more like $W^{1/4}$.

The calculated cratering curve for Divide basalt differs in that, while the yield effect in crater size is small, the optimum burial depth for a 1-Mt yield is approximately the same as for a 0.5-kt yield. In this case, the saturated rock provides a strong gas acceleration phase.

The increase in crater size due to gas acceleration can be separated easily from spalling by performing a throwout calculation at the end of the spalling process. Data points from these calculations are shown in Fig. 31 as crosses with a superscript s. The optimum depth of burial (scalewise) is very shallow for spall craters; this emphasizes the importance of the gas acceleration phase in cratering at the megaton level.

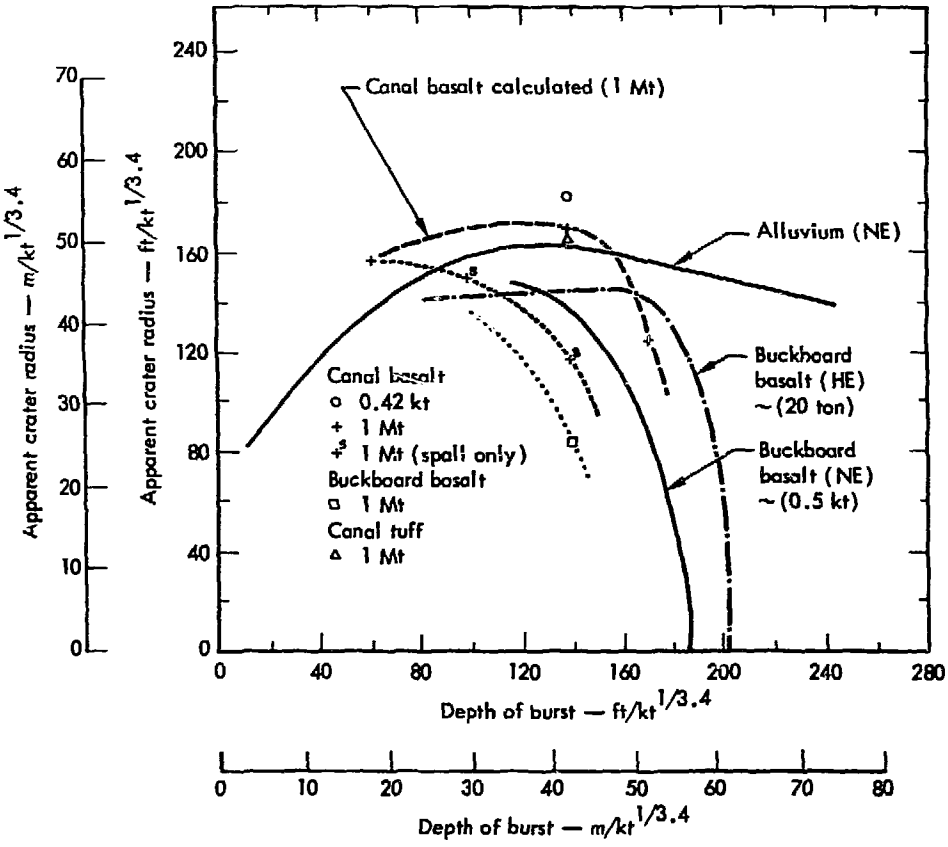

Fig. 31. Scaled crater radius curves.

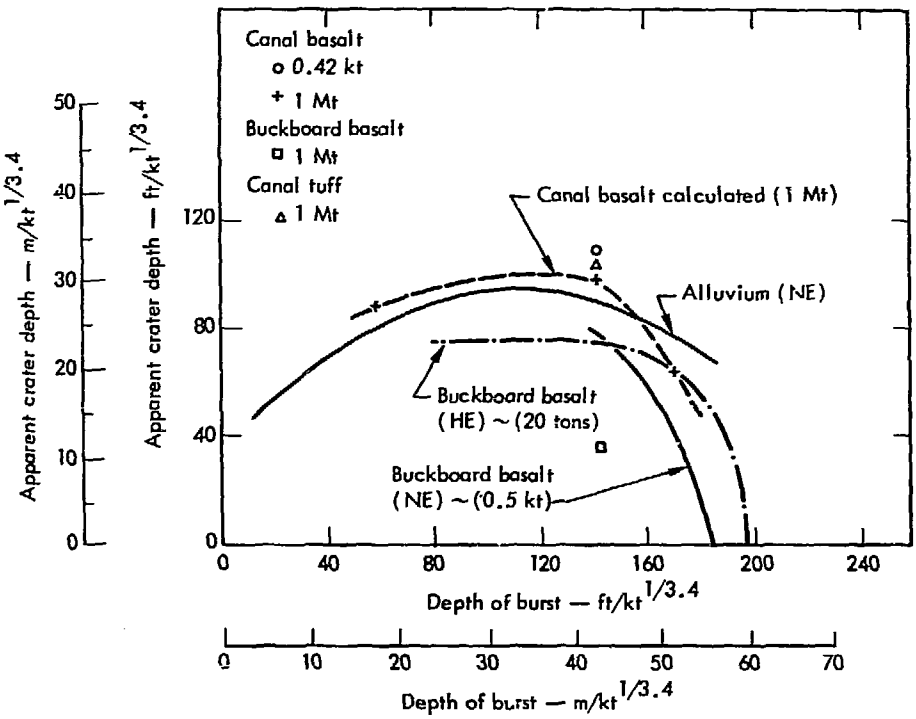

Fig. 32. Scaled crater depth curves.

Conclusions

By the calculational approach, the importance and relationship of material parameters to cratering efficiency in various media have been illustrated. The water content of the medium has been emphasized because it enhances the medium as a stress transmitter, decreases the material strength such that high velocities are maintained, and provides noncondensable gas in the cavity for a strong gas acceleration phase.

Using a systematic method in the development of the equation of state, the codes have reproduced the dynamic measurements made on various field experiments. The resulting crater calculations are in good agreement.

A cratering curve for Divide basalt is presented, illustrating the need for a strong gas acceleration phase at the megaton-yield level.

Improvements in the equation of state are needed along with improvements in the codes. High-pressure experimental data on the release paths of saturated rock are sorely needed. Constant improvements are being made in the calculational approach, in line with improved equation-of-state measurements. Hopefully, experimental data on the release paths of

saturated rocks will soon be available Also, plans are underway to include overburden in TENSOR by calculation of the initial stress field with the finite-element method.

Acknowledgments

The authors wish to thank Fran Peterson for her assistance in running the SOC code, John White for his help with the calculations, and Jim Shaw for his invaluable aid in running the TENSOR code.

References

1. G. Maechen and S. Sack, The Tensor Code, Lawrence Radiation Laboratory, Livermore, Rept. UCRL-7316 (1963).
2. J. T. Cherry and W. R. Hurdlow, "Numerical Simulation of Seismic Disturbances," Geophysics 31, 33 (1966).
3. M. L. Wilkins, Calculation of Elastic Plastic Flow, Lawrence Radiation Laboratory, Livermore, Rept. UCRL-7322 Rev. 1 (1969).
4. J. T. Cherry, "Computer Calculations of Explosion-Produced Craters," Int. J. Rock Mech. Min. Sci. 4, 1-22 (1967).
5. D. R. Stephens and E. M. Lilly, "Static PV Curves of Cracked and Consolidated Earth Materials to 40 Kilobars," Proceedings of Conference on Shock Metamorphism of Natural Materials, Greenbelt, Md., April 1966.
6. D. R. Stephens, E. M. Lilly, and H. Louis, "Pressure and Volume Equation of State of Consolidated and Fractured Rocks to 40 Kbars," Int. J. Rock Mech. Min. Sci. (to be published).
7. E. Chamberlain and G. Dante, Solid Cell P-V Test Interoceanic Canal Studies Route 17, U.S. Army Terrestrial Science Center, Hanover, N.H.
8. H. C. Heard, "The Influence of Environment on the Inelastic Behavior of Rocks," ANS Symposium on Engineering with Nuclear Explosives, 1970.
9. H. C. Heard, Lawrence Radiation Laboratory, Livermore, private communication.
10. R. L. Bjork, K. N. Kreyehagen, and G. H. Wagner, private communication.
11. J. Day, D. Murrell, and W. Sherman, Close In-Ground Motion, Earth Stress and Pore Pressure Measurement—Pre-Gondola I Series, PNE-1104, U.S. Army Nuclear Cratering Group, U.S. Army Corp of Engineers (1967).
12. M. D. Nordyke and M. M. Williamson, The Sedan Event, Lawrence Radiation Laboratory, Livermore, Rept. PNE-242F (1965).
13. W. S. Brown, J. J. Tanner, and K. L. DeVries, The Effect of Pressure on the Strength of Rock from Two Prospective Routes for an Interoceanic Canal, (W. S. Brown Inc., Salt Lake City, Utah, 1969).

Printed in USA. Available from the National Technical Information Center, National Bureau of Standards, U. S. Department of Commerce, Springfield, Virginia 22151
Price: Printed Copy $3.00; Microfiche $0.65.